PNAS RESEARCH ARTICLE | BIOCHEMISTRY

Structural basis for the recognition of the bacterial tyrosine kinase Wzc by its cognate tyrosine phosphatase Wzb

Sébastien Alphonse[a,1], Imane Djemil[b,1], Andrea Piserchio[a], and Ranajeet Ghose[a,b,c,d,2]

Edited by Natalie Ahn, University of Colorado Boulder, Boulder, CO; received January 31, 2022; accepted May 7, 2022

Bacterial tyrosine kinases (BY-kinases) comprise a family of protein tyrosine kinases that are structurally distinct from their functional counterparts in eukaryotes and are highly conserved across the bacterial kingdom. BY-kinases act in concert with their counteracting phosphatases to regulate a variety of cellular processes, most notably the synthesis and export of polysaccharides involved in biofilm and capsule biogenesis. Biochemical data suggest that BY-kinase function involves the cyclic assembly and disassembly of oligomeric states coupled to the overall phosphorylation levels of a C-terminal tyrosine cluster. This process is driven by the opposing effects of intermolecular autophosphorylation, and dephosphorylation catalyzed by tyrosine phosphatases. In the absence of structural insight into the interactions between a BY-kinase and its phosphatase partner in atomic detail, the precise mechanism of this regulatory process has remained poorly defined. To address this gap in knowledge, we have determined the structure of the transiently assembled complex between the catalytic core of the *Escherichia coli* (K-12) BY-kinase Wzc and its counteracting low–molecular weight protein tyrosine phosphatase (LMW-PTP) Wzb using solution NMR techniques. Unambiguous distance restraints from paramagnetic relaxation effects were supplemented with ambiguous interaction restraints from static spectral perturbations and transient chemical shift changes inferred from relaxation dispersion measurements and used in a computational docking protocol for structure determination. This structure presents an atomic picture of the mode of interaction between an LMW-PTP and its BY-kinase substrate, and provides mechanistic insight into the phosphorylation-coupled assembly/disassembly process proposed to drive BY-kinase function.

bacterial tyrosine kinase | low–molecular weight protein tyrosine phosphatase | solution NMR | relaxation dispersion | paramagnetic relaxation enhancement

Significance

This study provides a structural view of the recognition of a bacterial tyrosine kinase (BY-kinase) by its counteracting phosphatase. BY-kinase function has been proposed to entail the cyclic assembly/disassembly of an oligomer coupled to the phosphorylation level of a C-terminal tyrosine cluster (Y-cluster). The structure of the BY-kinase–phosphatase complex highlights the use of the same conserved element on the kinase for both oligomerization and phosphatase docking. This mode of interaction prevents phosphatase engagement and dephosphorylation before exceeding a critical threshold of Y-cluster phosphorylation necessary for oligomer disassembly. Reassembly occurs once the Y-cluster is sufficiently dephosphorylated by the phosphatase that is then excluded, thereby repriming the cycle. This phosphorylation-coupled assembly/disassembly process likely serves to temporally coordinate intra- and extracytoplasmic events.

The BY-kinase (bacterial tyrosine kinase) family of protein tyrosine kinases (PTKs) is highly conserved within the bacterial domain and regulates a variety of physiological processes (1–5). Most notable among these processes are the synthesis and export of the polysaccharide constituents of biofilms and capsules (2, 4) that are cytoprotective under environmental stress and contribute to the virulence of several pathogenic species (6, 7). In gram-negative bacteria, BY-kinases are anchored to the inner membrane through a two-pass transmembrane domain (TMD) that links a periplasmic domain (PD) to a C-terminal cytoplasmic catalytic domain (CD) (*SI Appendix*, Fig. S1*A*) (8). Through the association of the PD with the periplasmic component of the outer-membrane transporter Wza (9), BY-kinases form part of a platform (10) that spans both the outer and inner membranes. This assembly enables BY-kinases to influence two distinct processes, the synthesis and the export of polysaccharides, by interactions within both the cytoplasmic and the periplasmic compartments.

BY-kinase CDs (8, 11–13) differ significantly in sequence (14) and structure (15) from eukaryotic protein tyrosine kinases (ePTKs). Rather, they contain sequence elements and display structural folds characteristic of the P-loop ATPases (16) (*SI Appendix*, Fig. S1*A*). BY-kinase function has been linked to the autophosphorylation of a cluster of tyrosine residues (Y-cluster) located at the C terminus of the CD (*SI Appendix*, Fig. S1*A*) (17, 18) and its subsequent dephosphorylation by a counteracting protein tyrosine phosphatase (PTP) (19, 20). Unlike in many ePTKs, where activity is related to the phosphorylation states of specific regulatory residues (21), BY-kinase function appears to be driven by cycling between states where the Y-cluster is highly phosphorylated (Y-high) and those where the level of Y-cluster phosphorylation is greatly reduced (Y-low) (18, 22) through the catalytic activity of PTPs (23). The Y-low states assemble in an octameric ring to enable efficient autophosphorylation of the Y-cluster in an intermolecular fashion (8, 12). Successive rounds of phosphorylation and generation of Y-high states result in ring disassembly; the ring reassembles after multiple rounds of PTP-mediated dephosphorylation and recreation of the Y-low states. This phosphorylation-linked assembly/disassembly cycle, that may be conceptualized as a supramolecular conformational change, is central to the biological function of BY-kinases (23). This highlights the functional

Author contributions: S.A., I.D., and R.G. designed research; S.A., I.D., and A.P. performed research; S.A., A.P., and R.G. analyzed data; and S.A. and R.G. wrote the paper.

The authors declare no competing interest.

This article is a PNAS Direct Submission.

[1]S.A. and I.D. contributed equally to this work.

[2]To whom correspondence may be addressed. Email: rghose@ccny.cuny.edu.

This article contains supporting information online at http://www.pnas.org/lookup/suppl/doi:10.1073/pnas.2201800119/-/DCSupplemental.

Published June 23, 2022.

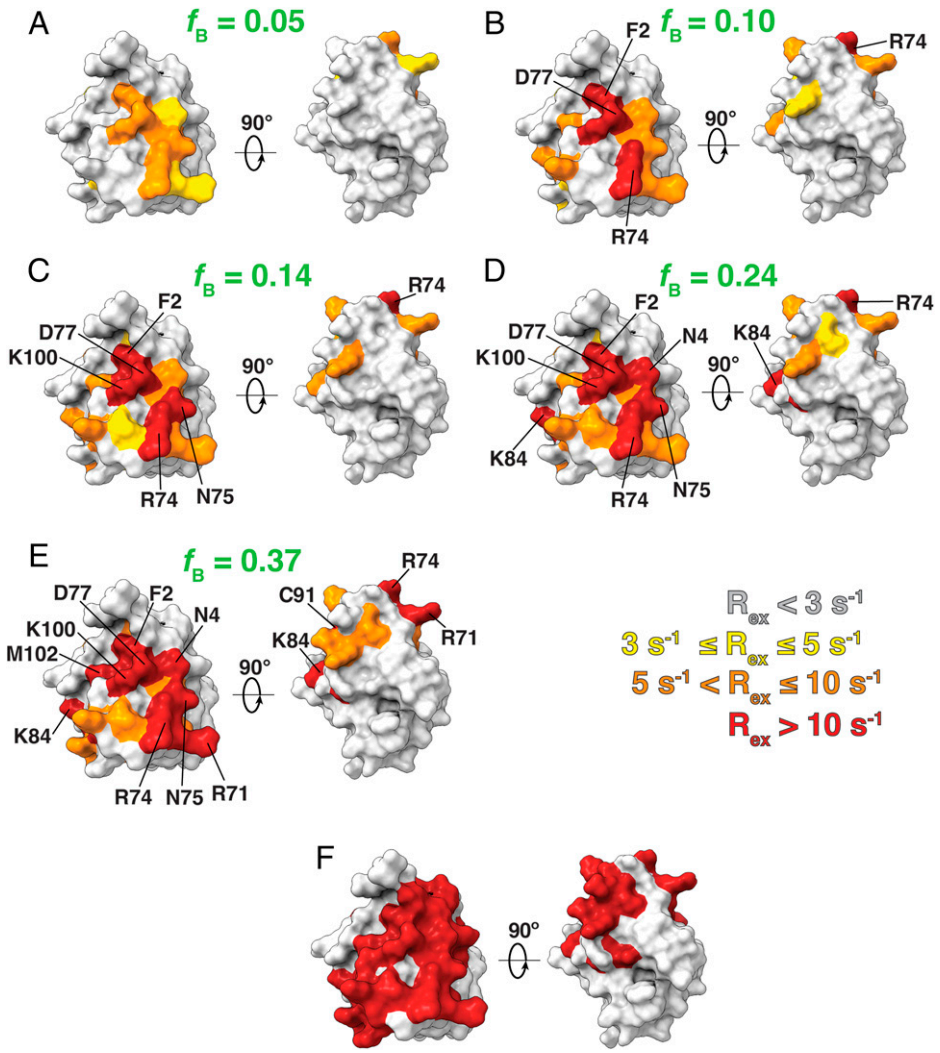

Fig. 1. R_{ex} values mapped onto the Wzb surface for various fractions of its $Wzc_{CD\Delta C}$-bound state. (*A–E*) $R_{ex} \leq 3\ s^{-1}$, gray; $3\ s^{-1} < R_{ex} \leq 5\ s^{-1}$, yellow; $5\ s^{-1} < R_{ex} \leq 10\ s^{-1}$, orange; $R_{ex} > 10\ s^{-1}$, red. (*F*) Wzb residues that show significant signal attenuation (>90%) in the presence of equimolar amounts of $Wzc_{CD\Delta C}$ are mapped onto the Wzb surface.

importance of maintaining the appropriate balance between self-interactions, to enable in trans autophosphorylation in BY-kinases, and those with a PTP, to facilitate dephosphorylation. While the atomic details of the self-interactions in BY-kinases have been highlighted by several structures (8, 12, 13), no such structural information is available for the interactions of the BY-kinases with their counteracting PTPs.

In prior studies, we had utilized NMR spectral perturbations to analyze the interactions between the CD of the *Escherichia coli* (K-12) BY-kinase, Wzc (Wzc_{CD}), and its cognate low–molecular weight PTP (LMW-PTP), Wzb (*SI Appendix*, Fig. S1*B*) (24). These studies suggested a conserved motif, ^{508}Glu−[Xxx]$_2$−Arg−[Xxx]$_2$−Arg^{514}, on the Wzc_{CD} α2-helix (*SI Appendix*, Fig. S1*A*), necessary for oligomerization (12), to also be involved in binding Wzb (24). Since those studies relied solely on NMR spectral perturbations, they did not resolve atomic details of the interactions that define the Wzc_{CD}–Wzb interface. Here, we utilize solution NMR methods to derive a variety of structural restraints to generate an atomic model of the Wzb–Wzc_{CD} complex that is validated through functional studies in vitro. This structure represents a detailed atomic view of the interaction between a BY-kinase and its cognate PTP, and indeed of any eukaryotic or prokaryotic LMW-PTP with its kinase partner, and provides critical insight into the role of this interaction in driving BY-kinase function.

Table 1. Apparent binding affinities of various $Wzc_{CD\Delta C}$ constructs for wild-type Wzb

Construct	K_D, μM
$Wzc_{CD\Delta C}$*	8.6 ± 0.6
$Wzc_{CD\Delta C,\Delta Cys}$	15.2 ± 0.6
$Wzc_{CD\Delta C,\Delta Cys,Val466Cys}$	8.9 ± 0.3
$Wzc_{CD\Delta C,\Delta Cys,Leu505Cys}$	43.8 ± 1.3
$Wzc_{CD\Delta C,\Delta Cys,Ser516Cys}$	11.3 ± 0.7
$Wzc_{CD\Delta C,\Delta Cys,Gln523Cys}$	16.9 ± 0.5
$Wzc_{CD\Delta C,\Delta Cys,Lys556Cys}$	7.3 ± 0.4

Determined through two-dimensional line-shape analyses of ^{13}C,^{1}H HMQC spectra assuming that the fast-relaxing component can be neglected.
*Determined by ITC, 10.7 ± 1.3 μM, or SPR, 5.1 ± 0.2 μM.

Results

We have previously shown that the disordered C-terminal tail of Wzc_{CD}, that includes the Y-cluster (residues Tyr705 to Lys720), is dispensable for its interaction with Wzb (24). A nonhydrolyzable phosphotyrosine mimic was also found to make minimal contributions to the binding free energy (24).

Therefore, we utilized a construct, $Wzc_{CD\Delta C}$, encoding the catalytic core of Wzc (Ser447 to Ala704) for our structural studies. We relied on two-dimensional line-shape analyses of resonances (25) in methyl $^{13}C,^{1}H$ heteronuclear multiple quantum coherence (HMQC) spectra of Wzb, labeled at the isoleucine (δ1), leucine and valine methyl positions (ILV-labeled), in the presence of increasing amounts of $Wzc_{CD\Delta C}$ (and its variants; described below) to quantify their mutual affinities. In the case of wild-type $Wzc_{CD\Delta C}$, this approach yields a K_D of 8.6 ± 0.6 μM (Table 1), comparable to that obtained from isothermal titration calorimetry (ITC) (10.7 ± 1.3 μM; *SI Appendix*, Fig. S2) and that previously obtained using surface plasmon resonance (SPR) measurements (5.1 ± 0.2 μM) (24).

We had previously noted extensive line broadening in $^{15}N,^{1}H$ transverse relaxation optimized spectroscopy (TROSY) spectra of Wzb in the presence of an equimolar amount of $Wzc_{CD\Delta C}$ (24), suggesting substantial exchange contributions attributable to the binding/unbinding process. Indeed, these effects prevented the use of spectral perturbations to precisely identify the $Wzc_{CD\Delta C}$-binding residues on Wzb. To identify Wzb "seed" residues that facilitate $Wzc_{CD\Delta C}$ recognition, we analyzed the transient chemical shift changes induced on $^{15}N,^{2}H$-labeled Wzb by the presence of substoichiometric amounts of $Wzc_{CD\Delta C}$ that manifest as exchange contributions to transverse relaxation (R_{ex}) in Carr-Purcell-Meiboom-Gill (CPMG) based ^{15}N relaxation dispersion measurements (26). While Wzb does not exhibit significant exchange in the absence of $Wzc_{CD\Delta C}$ (*SI Appendix*, Fig. S3*A*), specific regions display exchange effects in the presence of $Wzc_{CD\Delta C}$, and the corresponding R_{ex} values are enhanced by increasing concentrations of the latter (and the fraction of Wzb within the Wzb–$Wzc_{CD\Delta C}$ complex). That these R_{ex} values are induced by binding/unbinding processes involving $Wzc_{CD\Delta C}$ is reinforced by the fact that the limiting relaxation rates, $R_{2,eff}$s (∞) (inferred from the corresponding values at the highest field used, 1,000 Hz), in the fast pulsing regime for almost all residues (*SI Appendix*, Fig. S4 for representative examples) are linearly dependent on the bound fraction (f_B).

As shown in Fig. 1 *A–E*, both the number of Wzb residues that display significant R_{ex} values, and the values themselves, are enhanced with increasing f_B. The distribution of residues with substantial R_{ex} values plotted on the Wzb surface for f_B = 0.37 largely mirrors the spatial pattern of attenuations seen for the amide resonances of Wzb in the presence of an equimolar ratio of $Wzc_{CD\Delta C}$ (Fig. 1*F*) reported previously (24). At the lowest f_B value (0.05), F2, the catalytic C9 (on β1′; *SI Appendix*, Fig. S1*B*), and R74 (α3′) show statistically significant R_{ex} values >5 s^{-1}. At f_B = 0.24, the R_{ex} values for F2, C9, and R74, in addition to N75 and D77 (on the α3′–β3′ loop), I79 (on β3′), and M82 (on the β3′–α4′ loop), all exceed 15 s^{-1} (*SI Appendix*, Fig. S3). Within this group of residues, F2, R74, N75, and D77 are all significantly solvent-exposed and their substantial R_{ex} values suggest that they are proximal to, if not in direct contact, with $Wzc_{CD\Delta C}$ within the Wzb–$Wzc_{CD\Delta C}$ complex. These transient chemical shift changes (as reflected by the significant R_{ex} values) on Wzb were utilized (*SI Appendix*, *Materials and Methods* and Table S2 for details) to generate ambiguous interaction restraints (AIRs) in our structure calculation protocol discussed below.

To obtain a direct measure of distances between the interacting partners, we relied on the measurement of paramagnetic relaxation enhancement (PRE) effects induced on Wzb by spin-labeled $Wzc_{CD\Delta C}$ variants. First, the two native cysteines on $Wzc_{CD\Delta C}$ were mutated to Ser (Cys544Ser/Cys563Ser) to generate a cysteine-less background ($Wzc_{CD\Delta C,\Delta Cys}$) to which nonnative cysteines could be introduced, one at a time, for the subsequent attachment of a spin label (*SI Appendix*, Fig. S5). $Wzc_{CD\Delta C,\Delta Cys}$ expresses well and can be purified similarly as $Wzc_{CD\Delta C}$. The $^{15}N,^{1}H$ TROSY spectrum of this mutant displays well-dispersed resonances indicative of a folded protein and suggests the absence of any significant structural reorganization compared with wild-type $Wzc_{CD\Delta C}$ (*SI Appendix*, Fig. S6*A*) with chemical shift perturbations (average ± SD over all resonances excluding those of residues within a 6-Å radius of the mutation sites) of 0.04 ± 0.03 parts per million (ppm). That the structural changes caused by the double mutation are modest is further confirmed by an almost unchanged affinity of $Wzc_{CD\Delta C,\Delta Cys}$ toward Wzb (Table 1).

Given the substantial number of Wzb resonances that are broadened in the presence of equimolar amounts of $Wzc_{CD\Delta C}$, substoichiometric concentrations of spin-labeled $Wzc_{CD\Delta C}$ variants would be necessary for precise PRE measurements requiring thoughtful placement of the spin labels. The spin labels would have to be proximal to the α2-helix harboring the important $^{508}Glu-[Xxx]_2-Arg-[Xxx]_2-Arg^{514}$ motif for maximal effect while minimally perturbing native interactions. Additionally, they would have to be optimally distributed in space to provide sufficient nonredundant distance information for use in structure calculations. Five single-cysteine variants (Val466Cys, Leu505Cys, Ser516Cys, Gln523Cys, and Lys556Cys), distributed around the $^{508}Glu-[Xxx]_2-Arg-[Xxx]_2-Arg^{514}$ motif, were introduced into the $Wzc_{CD\Delta C,\Delta Cys}$ background (*SI Appendix*, Fig. S5). All variants express well and are properly folded as indicated by the corresponding $^{15}N,^{1}H$ TROSY spectra (*SI Appendix*, Fig. S6 *B–F*). The Wzb affinities of all variants, with the exception of $Wzc_{CD\Delta C,\Delta Cys,Leu505Cys}$ (Table 1), remain largely unchanged in comparison to $Wzc_{CD\Delta C}$. The $^{13}C,^{1}H$ HMQC spectra of Wzb display fast exchange in the presence of increasing amounts of $Wzc_{CD\Delta C,\Delta Cys,Leu505Cys}$, contrasting the slow-exchange regime seen for $Wzc_{CD\Delta C}$ and all other variants (*SI Appendix*, Fig. S7). Given the ∼5-fold reduction in affinity, and the likely related modification in its association dynamics, the $Wzc_{CD\Delta C,\Delta Cys,Leu505Cys}$ mutant was excluded from further analysis. The patterns of chemical shift perturbations of methyl resonances (*SI Appendix*, Fig. S8) of Wzb in the presence of the $Wzc_{CD\Delta C}$ variants suggest no significant modification in the overall modes of interaction compared with the wild-type species.

To generate spin-labeled single-cysteine variants of $Wzc_{CD\Delta C}$, we utilized a 3-(2-iodoacetamido)-proxyl spin label (IPSL) that covalently attaches to cysteine via a thioester bond. The efficiency of the spin labeling of ^{2}H-labeled $Wzc_{CD\Delta C}$ variants (for use in the NMR experiments) was confirmed by mass spectrometry; a successful labeling reaction is indicated by a mass increase of ∼198 Da for the IPSL-modified species (*SI Appendix*, Fig. S9 for a representative example). Four IPSL-labeled variants (Val466Cys, Ser516Cys, Gln523Cys, and Lys556Cys) were subsequently utilized to measure PREs induced on $^{2}H,^{15}N$-labeled Wzb. The appropriate attachment of the spin labels was confirmed by the pattern of signal attenuations seen in $^{15}N,^{1}H$ TROSY spectra of the spin-labeled $Wzc_{CD\Delta C}$ variants (*SI Appendix*, Fig. S10). Analyses of the patterns of perturbations of the amide resonances of Wzb in the presence of the reduced forms of the IPSL-labeled $Wzc_{CD\Delta C}$ mutants confirm that this covalent modification does not substantially alter their modes of interaction with Wzb (*SI Appendix*, Fig. S11).

Ratios of intensities of Wzb resonances in the presence of each of the four spin-labeled $Wzc_{CD\Delta C}$ variants in their paramagnetic (I_{para}) and diamagnetic (I_{dia}) states (*SI Appendix*, Fig. S12; refer to *SI Appendix*, *Materials and Methods* for

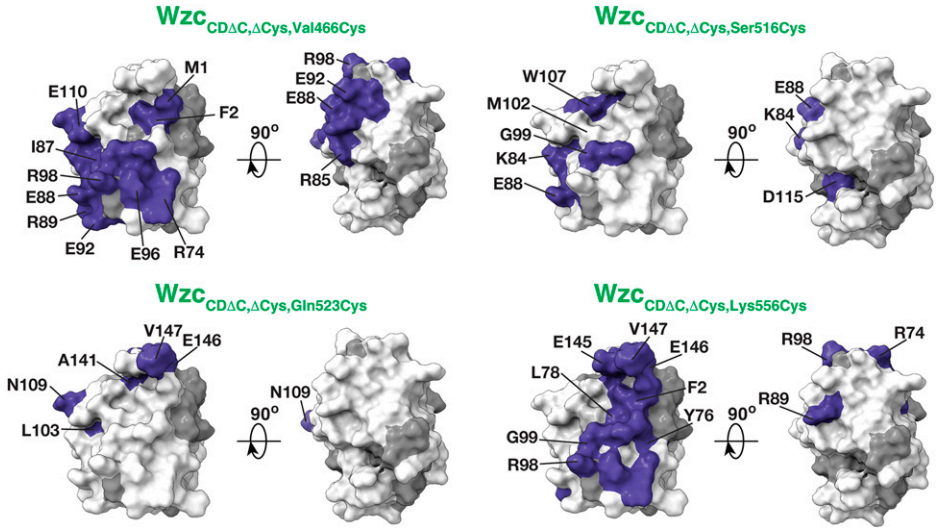

Fig. 2. PREs induced on Wzb in the presence of IPSL-labeled $Wzc_{CD\Delta C}$ variants. The ratios I_{para}/I_{dia} <0.7 are mapped onto the Wzb surface (in blue) for the Val466Cys, Ser516Cys, Gln523Cys, and Lys556Cys variants generated on the $Wzc_{CD\Delta C,\Delta Cys}$ background. Residues for which data could not be analyzed due to missing resonance assignments or spectral overlap are colored gray. Intensity ratios correspond to those measured for $^{2}H,^{15}N$-labeled Wzb in the presence of IPSL,^{2}H-labeled $Wzc_{CD\Delta C}$ variants in the following molar equivalents: $Wzc_{CD\Delta C,\Delta Cys,Val466Cys}$ (0.5), $Wzc_{CD\Delta C,\Delta Cys,Gln523Cys}$ (0.5), $Wzc_{CD\Delta C,\Delta Cys,Ser516Cys}$ (0.36), and $Wzc_{CD\Delta C,\Delta Cys,Lys556Cys}$ (0.34). Key perturbed residues are labeled.

experimental details) show distinct patterns, suggesting that the measured PREs encode significant nonredundant distance information. Residues with statistically significant reduction in intensity (I_{para}/I_{dia} < 0.7) mapped onto the surface of Wzb (Fig. 2) are localized within well-defined patches, implying that the transiently assembled complex is restricted to a single overall orientation, or a set of very similar orientations.

A set of 59 unambiguous distance restraints (listed in *SI Appendix*, Table S3 and illustrated in *SI Appendix*, Fig. S13) arising from the four spin-labeled sites on $Wzc_{CD\Delta C}$—Val466Cys, Ser516Cys, Gln523Cys, and Lys556Cys—was supplemented with the AIRs (*SI Appendix*, Table S2) obtained from the relaxation dispersion measurements on Wzb (described above) and our previously measured spectral perturbations on $Wzc_{CD\Delta C}$ (*SI Appendix*, Fig. S14) (24) and utilized in docking calculations using the HADDOCK suite (27, 28) to obtain the structure of the Wzb–$Wzc_{CD\Delta C}$ complex. The importance of the PRE-based unambiguous distance restraints is highlighted by the fact that their inclusion is crucial in obtaining a single dominant structural cluster ($Cluster_{ALL,1}$ and $Cluster_{PRE,1}$ with ∼53 and ∼59%, respectively, of the 400 refined structures; compare *SI Appendix*, Tables S4 and S5 with *SI Appendix*, Table S6). The overall characteristics of the protein interfaces calculated with or without AIRs are quite similar (*SI Appendix*, Fig. S15) but with the former set of calculations leading to more favorable HADDOCK scores. Therefore, unless otherwise stated, we focus exclusively on the structures that constitute $Cluster_{ALL,1}$ in the discussion below.

As previously noted, the α2-helix of $Wzc_{CD\Delta C}$, and the invariant Glu508/Arg511/Arg514 triad therein, has been predicted to play a crucial role in the recognition of Wzb (24). A statistical analysis of the 212 structures that constitute $Cluster_{ALL,1}$ suggests that $Wzc_{CD\Delta C}$ residues that comprise the interface (defined as those that lie within 4 Å of any Wzb residue; *SI Appendix*, Fig. S16) includes all three residues of the triad, together with the intervening Ser512 in all constituent structures. His518, Phe519, and Met522, all on α2, and Asn555 and Arg557, on the α3–β2 loop, are found at the interface in >80% models. The complementary interface on Wzb involves residues (found in >80% of the structures; *SI Appendix*, Fig. S16) of the N terminus (F2), the α3′–β3′ loop (D77), the α4′–β4′ loop (P95, R98, G99, K100), the β4′-strand (M102), the D loop (β4′–α5′ loop; H106, W107), and the C terminus (E145, Q146, V147). These same residues are also part of the protein–protein interface in the other major clusters, $Cluster_{ALL,2}$, $Cluster_{ALL,3}$, and $Cluster_{ALL,4}$ (*SI Appendix*, Fig. S16).

The interaction results in the burial of relatively modest surface areas of 757 and 747.2 Å^2 for $Wzc_{CD\Delta C}$ and Wzb, respectively, a likely explanation for their relatively weak interaction. Despite the presence of a significant number of polar residues at the interface, only seven intermolecular hydrogen bonds/salt bridges are consistently detected, of which only two involve Wzb side chains, D77 and R98, that form salt bridges with Asn555 and Glu508, respectively. The position corresponding to D77 is invariant in LMW-PTPs. The R98 position, though somewhat less conserved, is generally a basic (histidine or lysine) residue when substituted (*SI Appendix*, Fig. S17). Hydrogen bonds of the G99 and V147 main chains with Arg514 and Asp637 side chains, respectively, provide additional stability at the interface. These interactions are supplemented by those involving hydrophobic clusters on the two partners comprising H106 and W107 on Wzb and His518, Phe519, and Met522 on $Wzc_{CD\Delta C}$. In LMW-PTPs, the position corresponding to H106 is somewhat less conserved, though it is a histidine in a large number of cases; the W107 position is largely conserved or contains an aromatic or a large hydrophobic residue in cases of deviations (*SI Appendix*, Fig. S17). Key interfacial interactions are illustrated in Fig. 3.

To test whether the structure of the Wzb–$Wzc_{CD\Delta C}$ complex (missing the Y-cluster) is compatible with Y-cluster dephosphorylation, we utilized the MODELLER suite (29) to attach the C-terminal tail fragment (Tyr705 to Lys720) onto the docked structures (*SI Appendix*, *Materials and Methods* for details). Five of the six Y-cluster tyrosine residues (Tyr708, Tyr710, Tyr711, Tyr713, and Tyr715) can access the Wzb active site in optimal fashion within the complex. The distances of the -OH moieties of these residues from the thiol group of C9 and the guanidino group of R15, both part of the catalytic C–$[X]_5$–R–[S/T] motif (30), are within (or very close to) their optimal distances of 3.3

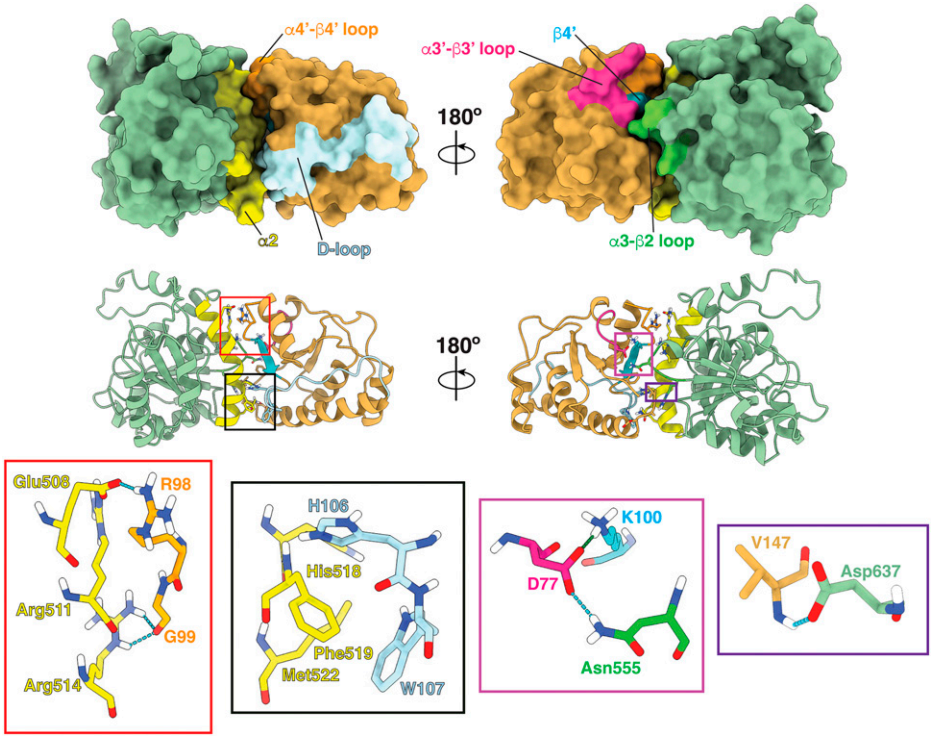

Fig. 3. Key interaction at the protein–protein interface in the Wzb–$Wzc_{CD\Delta C}$ complex. The structure of the lowest-energy model (from $Cluster_{ALL,1}$) is shown in surface (*Top*) and ribbon (*Middle*) representation. Interacting elements on each partner that comprise the interface are indicated. Expansions of specific regions (indicated by the colored rectangles) illustrating key interactions that stabilize the interface are shown (*Bottom*). The cyan dashed lines indicate intermolecular hydrogen bonds; the green dashed line indicates the intramolecular D77–K100 salt bridge discussed in the text.

and 2.6 Å (31, 32), respectively (*SI Appendix*, Fig. S18). In contrast, these distances deviate significantly for Tyr705, suggesting that the dephosphorylation of this residue, if it occurs at all, is expected to be highly inefficient. It is notable that Tyr705 is the only position on the Y-cluster that has been shown not to be autophosphorylated in Wzc (17).

We have previously demonstrated that a Glu508Ala/Arg511Ala/Arg514Ala mutant, where the conserved residues of the $^{508}Glu-[Xxx]_2-Arg-[Xxx]_2-Arg^{514}$ motif of Wzc_{CD} have been replaced by alanine, is severely compromised in its ability to interact with and be dephosphorylated by Wzb (24). Those results support the involvement of these residues in recognizing Wzb in line with our current structure. To test the complementary surface on Wzb, we mutated D77 and R98 (discussed above) individually to alanine. While the Wzb_{R98A} mutant expresses well and can be purified to homogeneity, the expression of the Wzb_{D77A} is suboptimal, suggesting that this mutation likely destabilizes the protein. We attributed this decreased stability to the loss of a salt bridge (Fig. 3) between

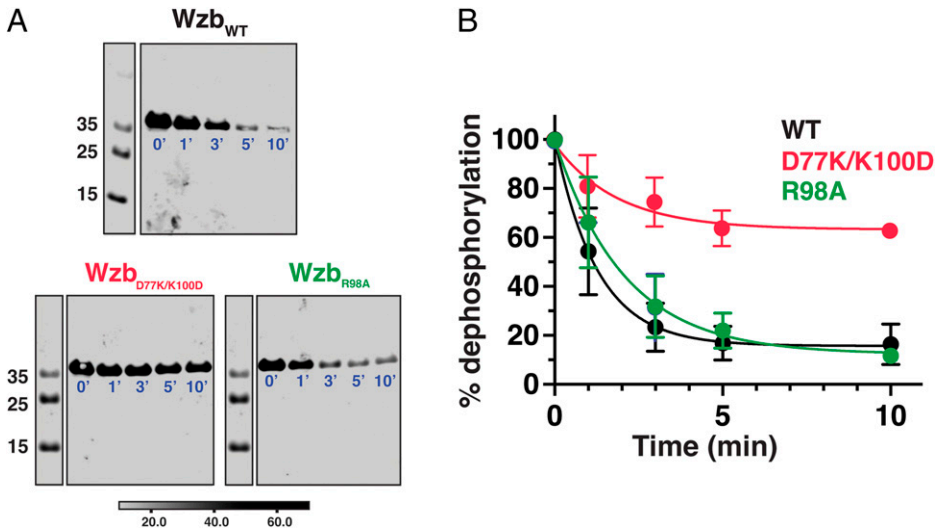

Fig. 4. Dephosphorylation of Wzc_{CD} by Wzb and variants. Reaction mixtures containing fully phosphorylated Wzc_{CD} were incubated for various time intervals (0, 1, 3, 5, and 10 min) with either wild-type (WT) Wzb or forms carrying double (D77K/K100D) or single (R98A) mutations at key sites at the protein–protein interface. Representative immunoblots for the time courses are shown in *A* and the corresponding fits to extract apparent dephosphorylation rates (normalized to 100%) are shown in *B*. Also shown are the positions of the molecular weight markers (in kDa). Note that the same lane corresponding to the molecular weight markers has been shown on the left hand sides of the time traces for each of the D77K/K100D and R98A mutants of Wzb on the bottom plots in panel A. This has been done to better guide the eye.

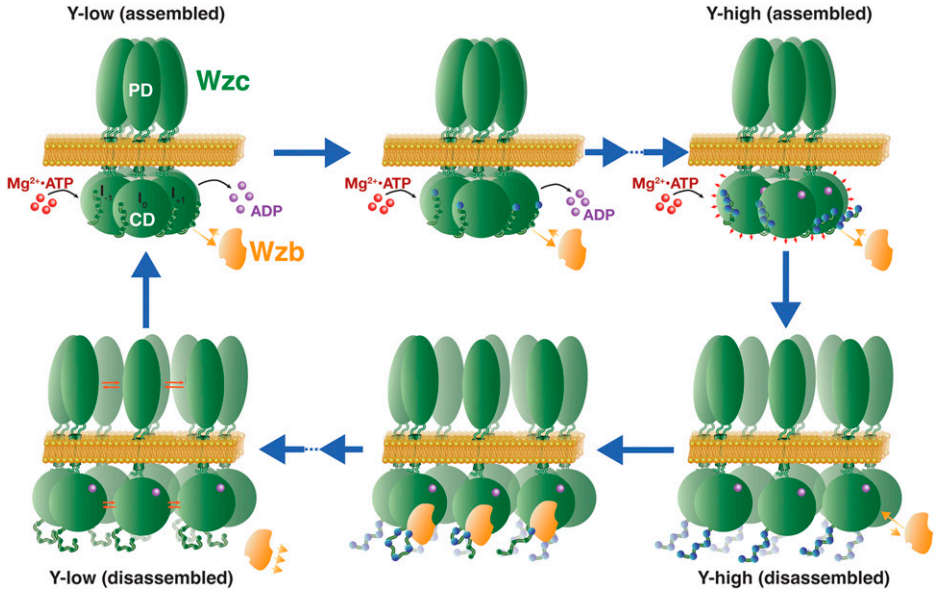

Fig. 5. Schematic illustration of the phosphorylation-coupled assembly/disassembly that drives BY-kinase function. At low levels of Y-cluster phosphorylation (Y-low assembled; represented as fully dephosphorylated for illustrative purposes), the cytoplasmic catalytic domain (Wzc_{CD}) of Wzc (green) forms an octameric ring. This assembly allows each Wzc_{CD} (I_0) subunit to simultaneously act as an enzyme, accommodating the Y-cluster of the preceding subunit (I_{-1}) at its active site, and as a substrate, inserting its own Y-cluster into the active site of the following subunit (I_{+1}). Oligomerization enables exchange of ATP·Mg^{2+} (dark red) for the bound ADP (purple), facilitating the progression to chemistry. At this stage, the diffusive binding of cytosolic Wzb (orange) is rendered inefficient due to the enhanced local concentration of Wzc_{CD} monomers in the context of the membrane-assembled species. Following several rounds of chemistry (phosphorylated tyrosine residues are indicated by blue spheres) and enhanced Y-cluster phosphorylation (Y-high assembled), the electrostatic repulsion (red arrows) increases above a critical threshold, making homotypic interactions between Wzc_{CD} monomers disfavored over heterotypic interactions with Wzb, that can engage the Wzc_{CD} monomers of the now disassembled ring (Y-high disassembled). After several rounds of Wzb-mediated dephosphorylation, the electrostatic repulsion is once again lowered below the critical threshold (Y-low disassembled), allowing the successful exclusion of Wzb and regeneration of the oligomeric state of Wzc_{CD} (Y-low assembled), thus reinitiating the cycle.

the side chains of D77 and the proximal K100, that is also highly conserved (*SI Appendix*, Fig. S17), in the mutant. To restore this salt bridge, we generated a charge-reversal variant, $Wzb_{D77K/K100D}$. This variant is also expected to be compromised in its ability to interact with and dephosphorylate Wzc_{CD}. The Wzb_{R98A} and $Wzb_{D77K/K100D}$ variants were compared with wild-type Wzb for their ability to dephosphorylate fully phosphorylated Wzc_{CD}. While Wzb_{R98A} can fully dephosphorylate Wzc_{CD}, it does so somewhat less efficiently than the wild-type enzyme (wild-type Wzb: 13.6 ± 2.3 s^{-1}; R98A: 9.1 ± 1.5 s^{-1}). Y-cluster dephosphorylation by $Wzb_{D77K/K100D}$ is severely compromised (1.8 ± 0.4 s^{-1}) and does not progress to completion (Fig. 4).

Discussion

The structure of the Wzb–$Wzc_{CD\Delta C}$ complex determined here not only reveals key structural features that enable molecular recognition between these two species but also provides a mechanistic framework to understand how the assembly/disassembly cycle correlates to Y-cluster phosphorylation states (8). As shown above, the α2-helix of Wzc_{CD} plays a key role in the recognition of Wzb. Indeed, interactions involving this helix, both polar and hydrophobic, appear to be conserved within BY-kinase/LMW-PTP pairs by comparing predicted structural interfaces between several related BY-kinase/LMW-PTP pairs from gram-negative species (*SI Appendix*, Fig. S19). As has been mentioned before, the α2-helix is also central to the formation of the oligomeric assembly (12) necessary to enable the active site of an enzyme-acting protomer to receive and phosphorylate the C-terminal Y-cluster of an adjoining substrate-acting subunit. Therefore, a competition for the α2-helix site between the homotypic and heterotypic interactions involving Wzc_{CD} monomers and Wzb, respectively, is expected. Thus, the processes of phosphorylation and dephosphorylation would need to be temporally separated for maximal efficiency. We suggest that this is achieved through the intricate mechanism illustrated in Fig. 5. As mentioned before, Wzc_{CD} is the cytosolic domain of a protein that is embedded in the bacterial inner membrane (8) (*SI Appendix*, Fig. S1*A*). Indeed, all BY-kinases need to form a membrane-associated species for activity (5). This arrangement results in the formation of an octamer through interactions between Wzc_{CD} monomers (8), supplemented by extracytoplasmic interactions, in the absence of Y-cluster phosphorylation. This membrane-bound assemblage greatly enhances the local concentration of Wzc_{CD} monomers and shields the α2-site from diffusion-controlled access by the wholly cytosolic Wzb. This allows phosphorylation to proceed [likely in sequence from the C terminus to the N terminus (8) of the Y-cluster] without the counteracting effects of premature Wzb-driven dephosphorylation. Once the Y-cluster is sufficiently phosphorylated, the homotypic affinity between Wzc_{CD} monomers is reduced due to strong electrostatic repulsion resulting from the significant accumulation of negative charge on the Y-cluster. When this repulsion exceeds a certain critical threshold, predicted to be at about four phosphorylated tyrosine residues based on functional data (8), the Wzc_{CD} monomers are pushed apart, allowing Wzb to successfully outcompete the intra-Wzc_{CD} interactions and dock at the α2-site to initiate dephosphorylation. After the dephosphorylation of a sufficient number of Y-cluster tyrosines, the repulsion between Wzc_{CD} monomers decreases below the critical threshold, allowing their reassociation and the successful exclusion of Wzb, thereby reinitiating the cycle. It has also been suggested that oligomerization of Wzc_{CD} monomers is necessary to enable the exchange of product adenosine diphosphate (ADP) for substrate adenosine triphosphate (ATP) (33). Given that Wzc_{CD} possesses significant ATPase activity (34), oligomerization would have to precede ATP binding to prevent futile hydrolysis. Specific features within the α2-helix have also been suggested to be coupled to that

process (33). Thus, this helix appears to be a central hub in coordinating multiple temporally regulated processes, and represents, what appears to be, part of an intricate timing mechanism that likely serves to couple intra- and extracytoplasmic events necessary for polysaccharide synthesis and export. It is notable that the region of Wzc that we suggest plays a key role in driving the proposed temporal regulation shows broad conservation in orthologs across the bacterial kingdom (*SI Appendix*, Fig. S20). While further studies are needed to test this "molecular stopwatch" hypothesis, and the role of BY-kinases therein, clues of its existence may be found in several gram-positive bacteria, for example *Staphylococcus aureus* (35) and *Streptococcus pneumoniae* (36, 37), where critical cellular processes appear to be coordinated through BY-kinase activity. Though direct experimental evidence of similar effects in gram-negative species is currently lacking, it has been shown that perturbations in the native Wzc in *E. coli* K30 (Wzc_{K30}) uncouple the dual process of the synthesis of capsular polysaccharides and their export to the cell surface (38).

In addition to generating testable hypotheses about BY-kinase regulation, the current study also illustrates key structural features of molecular recognition involving an LMW-PTP. Whether the engagement mode seen here is general for interactions involving LMW-PTPs is unclear. Based on the conservation of the LMW-PTP fold from bacteria to humans (39) and the resulting diversity of interactions, one would expect this not to be the case. Indeed, given the absence of additional regulatory domains that decorate their high–molecular weight counterparts (40), LMW-PTPs have likely evolved varied interaction modes based on their particular cellular context. For example, MptpA, one of the two LMW-PTPs encoded by *Mycobacterium tuberculosis*, that lacks BY-kinases, appears to utilize a different interaction mode to engage the atypical tyrosine kinase PtkA (41). Nevertheless, for cognate BY-kinase/LMW-PTP pairs, we expect that the interactions involving the α2-helix of the kinase and the corresponding elements of the phosphatase are conserved and represent a general mode of molecular recognition. This common mode may be supplemented by additional interactions in different BY-kinase/LMW-PTP pairs. For example, the interaction between D77 and Asn555, deemed important in the present case, appears not to be conserved in the other related pairs illustrated in *SI Appendix*, Fig. S19. While the phosphatase residue (D77 in Wzb) is fully conserved, the corresponding residue on the kinase (Asn555 in Wzc) is not conserved for the cases shown (also see *SI Appendix*, Fig. S20). That it is possible to compensate for this supplementary interaction is suggested by the fact Wzb can complement Wzb_{K30} within the group 1 capsule production system of *E. coli* K30 (38). Indeed, reinforcement of a primary mode of recognition by additional interactions would not be unusual for PTPs. For example, the MAP kinase regulatory HePTP recognizes the related p38 and ERK kinases through a kinase interaction motif but specificity toward p38 results from additional interactions involving a kinase specificity sequence (42). However, more extensive pairwise structure-based analyses on bona fide functional BY-kinase/LMW-PTP partners across the bacterial kingdom are needed to parse general recognition modes from system-specific nuances. These bioinformatic/computational analyses would have to be validated through additional experimental structures, most importantly for a representative pair from a gram-positive species to complement the present work.

The LMW-PTPs represent an ancient, but poorly studied, class of protein phosphatases (39), and molecular interactions involving them are suitable targets for the design of pharmaceuticals ranging from antimicrobials (43) to antidiabetics (44). Beyond insight into BY-kinase regulation, we expect that our current studies will provide a general approach to studying molecular recognition in a broader class of LMW-PTPs.

Materials and Methods

Protein Expression and Purification. All constructs (and variants) of the catalytic domain of *E. coli* (K-12) Wzc (447 to 725; Wzc_{CD}), its truncated form (lacking the C-terminal tail, 447 to 704; $Wzc_{CD\Delta C}$), and full-length *E. coli* (K-12) Wzb were expressed and purified using protocols described at length in *SI Appendix, Materials and Methods*. A list of constructs used in this study is given in *SI Appendix*, Table S1.

NMR Experiments. All NMR experiments were recorded at 25 °C using Bruker Avance III spectrometers operating at 600, 700, or 800 MHz, all equipped with cryogenic probes capable of applying pulsed-field gradients along the *z* axis. Additional details of specific experiments and methodology may be found in *SI Appendix, Materials and Methods*.

Computational Protocols. Structure calculations were performed using ambiguous interaction restraints (*SI Appendix*, Table S2) from the measurement of transient chemical shifts (Wzb) and static spectral perturbations ($Wzc_{CD\Delta C}$) in combination with PRE-based unambiguous restraints (*SI Appendix*, Table S3) using the HADDOCK suite (27). Procedures used for the preparation of starting structures for Wzc_{CD} and Wzb, generation of experimental restraints, and computational protocols used are described in detail in *SI Appendix, Materials and Methods*.

Protein Dephosphorylation Assays. The ability of phosphorylated Wzc_{CD} to be dephosphorylated by wild-type Wzb and corresponding D77K/K100D and R98A mutants was tested by immunoblotting using the monoclonal anti-phosphotyrosine antibody PY20 (dilution 1:5,000; Invitrogen). Experimental details are provided in *SI Appendix, Materials and Methods*.

Data Availability. The HADDOCK-generated structural ensembles are available through the Open Science Framework (OSF), (https://osf.io/fmwda/) (45). All other study data are included in the article and/or *SI Appendix*.

ACKNOWLEDGMENTS. This work was supported by NSF Grant MCB1937937. NMR measurements were carried out in the CUNY Advanced Science Research Center (ASRC) Biomolecular NMR Facility and at the New York Structural Biology Center (NYSBC). The NMR facilities at the NYSBC are supported by NIH Grants OD016432 and OD018509. We thank Dr. Kaushik Dutta (NYSBC) for help at the initial stages of this project, Dr. Christophe Grangeasse (Molecular Microbiology and Structural Biochemistry, Lyon) and Mr. Fatlum Hajredini (The City College of New York) for useful discussions, Dr. James Aramini (CUNY ASRC) for implementing some of the NMR experiments utilized in this study, and Dr. Brian Kloss (NYSBC) for the kind gift of the anti-phosphotyrosine antibody.

Author affiliations: [a]Department of Chemistry and Biochemistry, The City College of New York, New York, NY 10031; [b]PhD Program in Biochemistry, The Graduate Center of The City University of New York (CUNY), New York, NY 10016; [c]PhD Program in Chemistry, The Graduate Center of CUNY, New York, NY 10016; and [d]PhD Program in Physics, The Graduate Center of CUNY, New York, NY 10016

1. J. D. Chao, D. Wong, Y. Av-Gay, Microbial protein-tyrosine kinases. *J. Biol. Chem.* **289**, 9463–9472 (2014).
2. C. Grangeasse, S. Nessler, I. Mijakovic, Bacterial tyrosine kinases: Evolution, biological function and structural insights. *Philos. Trans. R. Soc. Lond. B Biol. Sci.* **367**, 2640–2655 (2012).
3. L. Shi, A. Kobir, C. Jers, I. Mijakovic, Bacterial protein-tyrosine kinases. *Curr. Proteomics* **7**, 188–194 (2010).
4. D. C. Lee, Z. Jia, Emerging structural insights into bacterial tyrosine kinases. *Trends Biochem. Sci.* **34**, 351–357 (2009).
5. C. Grangeasse, A. J. Cozzone, J. Deutscher, I. Mijakovic, Tyrosine phosphorylation: An emerging regulatory device of bacterial physiology. *Trends Biochem. Sci.* **32**, 86–94 (2007).
6. C. Schwechheimer *et al.*, A tyrosine phosphoregulatory system controls exopolysaccharide biosynthesis and biofilm formation in *Vibrio cholerae*. *PLoS Pathog.* **16**, e1008745 (2020).

7. C. M. Ernst *et al.*, Adaptive evolution of virulence and persistence in carbapenem-resistant *Klebsiella pneumoniae*. *Nat. Med.* **26**, 705–711 (2020).
8. Y. Yang *et al.*, The molecular basis of regulation of bacterial capsule assembly by Wzc. *Nat. Commun.* **12**, 4349 (2021).
9. C. Dong *et al.*, Wza the translocon for *E. coli* capsular polysaccharides defines a new class of membrane protein. *Nature* **444**, 226–229 (2006).
10. R. F. Collins *et al.*, The 3D structure of a periplasm-spanning platform required for assembly of group 1 capsular polysaccharides in *Escherichia coli*. *Proc. Natl. Acad. Sci. U.S.A.* **104**, 2390–2395 (2007).
11. D. C. Lee, J. Zheng, Y. M. She, Z. Jia, Structure of *Escherichia coli* tyrosine kinase Etk reveals a novel activation mechanism. *EMBO J.* **27**, 1758–1766 (2008).
12. E. Bechet *et al.*, Identification of structural and molecular determinants of the tyrosine-kinase Wzc and implications in capsular polysaccharide export. *Mol. Microbiol.* **77**, 1315–1325 (2010).
13. V. Olivares-Illana *et al.*, Structural basis for the regulation mechanism of the tyrosine kinase CapB from *Staphylococcus aureus*. *PLoS Biol.* **6**, e143 (2008).
14. S. K. Hanks, T. Hunter, Protein kinases 6. The eukaryotic protein kinase superfamily: Kinase (catalytic) domain structure and classification. *FASEB J.* **9**, 576–596 (1995).
15. S. W. Cowan-Jacob, Structural biology of protein tyrosine kinases. *Cell. Mol. Life Sci.* **63**, 2608–2625 (2006).
16. F. Jadeau *et al.*, Identification of the idiosyncratic bacterial protein tyrosine kinase (BY-kinase) family signature. *Bioinformatics* **24**, 2427–2430 (2008).
17. C. Grangeasse, P. Doublet, A. J. Cozzone, Tyrosine phosphorylation of protein kinase Wzc from *Escherichia coli* K12 occurs through a two-step process. *J. Biol. Chem.* **277**, 7127–7135 (2002).
18. A. Paiment, J. Hocking, C. Whitfield, Impact of phosphorylation of specific residues in the tyrosine autokinase, Wzc, on its activity in assembly of group 1 capsules in *Escherichia coli*. *J. Bacteriol.* **184**, 6437–6447 (2002).
19. C. Grangeasse *et al.*, Functional characterization of the low-molecular-mass phosphotyrosine-protein phosphatase of *Acinetobacter johnsonii*. *J. Mol. Biol.* **278**, 339–347 (1998).
20. C. Vincent *et al.*, Cells of *Escherichia coli* contain a protein-tyrosine kinase, Wzc, and a phosphotyrosine-protein phosphatase, Wzb. *J. Bacteriol.* **181**, 3472–3477 (1999).
21. T. J. Boggon, M. J. Eck, Structure and regulation of Src family kinases. *Oncogene* **23**, 7918–7927 (2004).
22. B. Obadia *et al.*, Influence of tyrosine-kinase Wzc activity on colanic acid production in *Escherichia coli* K12 cells. *J. Mol. Biol.* **367**, 42–53 (2007).
23. E. Bechet *et al.*, Tyrosine-kinases in bacteria: From a matter of controversy to the status of key regulatory enzymes. *Amino Acids* **37**, 499–507 (2009).
24. D. B. Temel *et al.*, Regulatory interactions between a bacterial tyrosine kinase and its cognate phosphatase. *J. Biol. Chem.* **288**, 15212–15228 (2013).
25. C. A. Waudby, A. Ramos, L. D. Cabrita, J. Christodoulou, Two-dimensional NMR lineshape analysis. *Sci. Rep.* **6**, 24826 (2016).
26. J. P. Loria, M. Rance, A. G. Palmer, A relaxation-compensated Carr-Purcell-Meiboom-Gill sequence for characterizing chemical exchange by NMR spectroscopy. *J. Am. Chem. Soc.* **121**, 2331–2332 (1999).
27. C. Dominguez, R. Boelens, A. M. Bonvin, HADDOCK: A protein-protein docking approach based on biochemical or biophysical information. *J. Am. Chem. Soc.* **125**, 1731–1737 (2003).
28. E. Karaca, A. S. Melquiond, S. J. de Vries, P. L. Kastritis, A. M. Bonvin, Building macromolecular assemblies by information-driven docking: Introducing the HADDOCK multibody docking server. *Mol. Cell. Proteomics* **9**, 1784–1794 (2010).
29. N. Eswar, D. Eramian, B. Webb, M. Y. Shen, A. Sali, Protein structure modeling with MODELLER. *Methods Mol. Biol.* **426**, 145–159 (2008).
30. D. Barford, Z. Jia, N. K. Tonks, Protein tyrosine phosphatases take off. *Nat. Struct. Biol.* **2**, 1043–1053 (1995).
31. X. Wang, Q. Ma, Wzb of *Vibrio vulnificus* represents a new group of low-molecular-weight protein tyrosine phosphatases with a unique insertion in the W-loop. *J. Biol. Chem.* **296**, 100280 (2021).
32. G. Hagelueken, H. Huang, I. L. Mainprize, C. Whitfield, J. H. Naismith, Crystal structures of Wzb of *Escherichia coli* and CpsB of *Streptococcus pneumoniae*, representatives of two families of tyrosine phosphatases that regulate capsule assembly. *J. Mol. Biol.* **392**, 678–688 (2009).
33. F. Hajredini, A. Piserchio, R. Ghose, Long-range dynamic correlations regulate the catalytic activity of the bacterial tyrosine kinase Wzc. *Sci. Adv.* **6**, eabd3718 (2020).
34. D. Soulat *et al.*, Tyrosine-kinase Wzc from *Escherichia coli* possesses an ATPase activity regulated by autophosphorylation. *FEMS Microbiol. Lett.* **274**, 252–259 (2007).
35. M. Rausch *et al.*, Coordination of capsule assembly and cell wall biosynthesis in *Staphylococcus aureus*. *Nat. Commun.* **10**, 1404 (2019).
36. R. Nakamoto *et al.*, The bacterial tyrosine kinase system CpsBCD governs the length of capsule polymers. *Proc. Natl. Acad. Sci. U.S.A.* **118**, e2103377118 (2021).
37. J. Nourikyan *et al.*, Autophosphorylation of the bacterial tyrosine-kinase CpsD connects capsule synthesis with the cell cycle in *Streptococcus pneumoniae*. *PLoS Genet.* **11**, e1005518 (2015).
38. A. N. Reid, C. Whitfield, Functional analysis of conserved gene products involved in assembly of *Escherichia coli* capsules and exopolysaccharides: Evidence for molecular recognition between Wza and Wzc for colanic acid biosynthesis. *J. Bacteriol.* **187**, 5470–5481 (2005).
39. A. Caselli *et al.*, Low molecular weight protein tyrosine phosphatase: Multifaceted functions of an evolutionarily conserved enzyme. *Biochim. Biophys. Acta* **1864**, 1339–1355 (2016).
40. N. K. Tonks, Protein tyrosine phosphatases: From genes, to function, to disease. *Nat. Rev. Mol. Cell Biol.* **7**, 833–846 (2006).
41. T. Stehle *et al.*, The apo-structure of the low molecular weight protein-tyrosine phosphatase A (MptpA) from *Mycobacterium tuberculosis* allows for better target-specific drug development. *J. Biol. Chem.* **287**, 34569–34582 (2012).
42. A. Piserchio *et al.*, Docking interactions of hematopoietic tyrosine phosphatase with MAP kinases ERK2 and p38α. *Biochemistry* **51**, 8047–8049 (2012).
43. L. Fanzani *et al.*, *Mycobacterium tuberculosis* low molecular weight phosphatases (MPtpA and MPtpB): From biological insight to inhibitors. *Curr. Med. Chem.* **22**, 3110–3132 (2015).
44. S. M. Stanford *et al.*, Diabetes reversal by inhibition of the low-molecular-weight tyrosine phosphatase. *Nat. Chem. Biol.* **13**, 624–632 (2017).
45. S. Alphonse, Wzb_Wzc_Complex_PNAS2022. Open Science Framework. https://osf.io/fmwda/. Deposited 9 June 2022.